Article

Reduced Graphene Oxide/Barium Ferrite Ceramic Nanocomposite Synergism for High EMI Wave Absorption

Ramy Sadek, Mohammad S. Sharawi, Charles Dubois, Hesham Tantawy, and Jamal Chaouki*

Read Online

ACCESS | Metrics & More | Article Recommendations

ABSTRACT: The developed nanocomposite exhibits significantly enhanced shielding performance due to the synergistic effect of high dielectric and magnetic loss materials, which modifies the material's impedance and improves its absorption ability. Different weight percentages (0, 1, 5, 10, 15, 20, and 25 wt %) of thermally treated chemically reduced graphene oxide (TCRGO) were combined with two types of magnets, barium hexaferrite (BF) and magnetite (MAG), using a dry powder compaction technique to produce binary ceramic nanocomposite sheets. The shielding performance of a 1 mm thick compressed nanoceramic sheet over the X-band was evaluated using a vector network analyzer. The 25% TCRGO showed high shielding performance for both BF and MAG, while BF had a total shielding efficiency (SET) that exceeded MAG by 130%. The SET of 25 wt % TCRGO/BF was 52 dB, with a 41 dB absorption shielding efficiency (SEA). Additionally, the effect of different levels of incident electromagnetic wave power (0.001−1000 mW) at various thicknesses (1, 2, and 5 mm) was explored. At 1000 mW, the 5 mm TCRGO/BF had an SET of 99 dB, an SEA of 91 dB, and a reflection shielding efficiency (SER) of 8 dB. The use of BF as a hard magnet paired with TCRGO exhibited excellent and stable electromagnetic shielding performance.
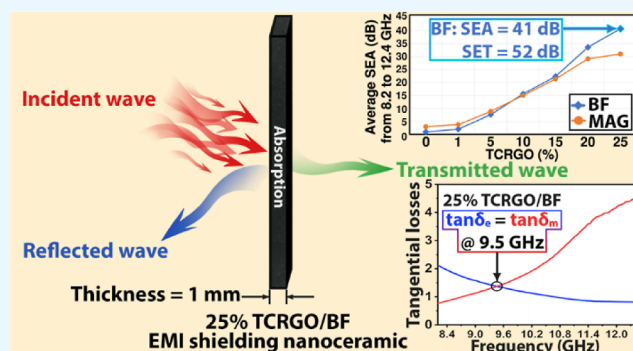
1. INTRODUCTION

Twenty first century is known as the "era of technology," which comes with electromagnetic interference (EMI) pollution that affects human health and interrupts the normal performance of electronic devices.[1−3] As a countermeasure to the increasing EMI problems, the use of EMI shielding materials rose due to the application of traditional heavy conductive shielding agents (e.g., sheet metal, metallic screen, and metallic foam) as well as advanced lightweight shielding materials (e.g., conductive polymers, magnetic, and conductive materials). Researchers began developing advanced shielding materials by manipulating the shielding mechanism parameters based on the dielectric and magnetic loss properties of the applied materials, offering the ability to control the absorption and reflection properties facing the incident electromagnetic waves to cover a wide variety of applications.[4] Barium hexaferrite (BF, $BaFe_{12}O_{19}$) is categorized as a hard magnet known for its high permeability, low cost, high Curie temperature, large intrinsic magnetic anisotropy, outstanding chemical stability, corrosion resistance, and large saturation magnetization.[5,6] Therefore, BF was applied in various applications, such as permanent magnets, recording media, and EMI shielding.[7] Unfortunately, its high density and low dielectric loss limit its use when EMI absorption becomes a concern.[8,9] Magnetite (MAG) is another metal-oxide candidate extensively studied for its exceptional

magnetic characteristics.[10−12] However, it faces similar drawbacks as BF, and in addition, it is easily oxidized and affected by Snoek's limit over the microwave frequencies (300 MHz to 300 GHz), which causes a sudden decline in permeability as the resonance frequency rises.[13,14] Previous studies show that magnetic metals, like magnetic ceramics, are promising EMI shielding materials.[15−17] Ceramics are favored over polymers, carbon foam, and carbon film as EMI shielding agents when high temperatures and oxidizing environments become a concern.[18] Still, their poor conductivity characteristics prevent them from being efficient in absorbing EMI shielding materials.[19] To overcome their limitations, BF and MAG were widely investigated through doping or in combination with other conductive materials to enhance their permittivity and tune their impedance, promoting their shielding efficiency (SE).[20−22]

On the other hand, conductive carbon-based shielding materials, such as reduced graphene oxide (RGO) and carbon nanotubes (CNTs), have low density and high dielectric loss, making them good electromagnetic wave absorbers.[23−26] Since it was difficult to offer a shielding material with good magnetic and dielectric losses, composites attracted researchers' interest in surpassing the limitations of the individual material and offering a wide variety of combinations to promote composite-shielding capabilities by fine tuning its magnetic and dielectric losses.[27−30] RGO has shown potential as a shielding agent among all carbonaceous materials due to its excellent conductivity and high surface area. In addition, its preparation using the top-down chemical synthesis approach had the advantage of being easily processed with a high yield, making it a promising candidate in many composites.[31−33] The enhancement reached through the formation of ceramic composites depends on the synergistic effect of dielectric and magnetic losses, which promote interfacial polarization and charge transfer, leading to an effective EMI ceramic sheet absorber.[34,35] This phenomenon provides composites with different permittivity and permeability values, which rely on the ratio between conductive and magnetic particles altering their impedance and raising their absorption shielding performance besides the consistent arrangement of minute nanoparticles.[36−38] The known ceramic formation techniques are slip casting,[39] additive manufacturing,[40] and technical ceramics.[41,42] The technical ceramic technique is widely used for dry powder processing into the required shape via mechanical or hydraulic powder compacting presses selected for the necessary force and powder fill depth. The creation of the basic shape of a component is achieved by compacting powder material through the application of external pressure using either single-action or double-action compaction techniques.[43] The powder mechanical mixing is an important step before powder compaction to facilitate the process and provide a homogenous blend between the ceramic composite constituents. The ball mill and traditional pestle and mortar are commonly used to offer the homogenous blend demanded.[44,45] Regarding the mechanical mixing approach, the ball mill method is a high-energy process that has a significant influence on the micro/nanostructure of the composite. It is able to mechanically exfoliate the graphite into high defected graphene sheets.[46,47] Consequently, this technique will alter the tailored thermally treated chemically reduced graphene oxide (TCRGO) characteristics and lead to an inaccurate evaluation after the composite formation. Therefore, the use of a pestle and mortar will minimize this drawback and provide the required nanocomposite homogeneity.

This study covers a binary ceramic nanocomposite based on a powder mixing compaction technique using a pestle and mortar by adding the specially prepared RGO (i.e., TCRGO) with different loadings to the metal oxides. BF as a hard magnet and MAG as a soft magnet were prepared using the coprecipitation method. The tailored TCRGO is prepared by developing a two-step protocol through chemical reduction followed by thermal treatment at 200 °C under vacuum for 4 h. The reflection, absorption, and total shielding efficiencies (SER, SEA, and SET) were evaluated via a vector network analyzer (VNA) over the X-band from 8.2 to 12.4 GHz. The dielectric and magnetic parameters (i.e., relative permittivity and permeability) were estimated by using the Keysight N1500A materials measurement software suite[48] and applying the measurement model named "reflection/transmission μ and

ε polynomial fit model" which is based on an iterative technique developed by Bartley et al.[49] Moreover, the study aims to evaluate the behavior of the optimized TCRGO percentage at various thicknesses (i.e., 1, 2, and 5 mm) under different levels of electromagnetic wave power covering 0.001−1000 mW. The study reveals the scientific debate between the BF and MAG in RGO nanocomposites and offers a solution to enhance the ceramics' EMI absorption efficiency by offering an optimized, lightweight, feasible binary nanocomposite material with a high shielding performance, which becomes a potential target as a filler for several applications, such as coatings, foams, adhesives, polymeric resins, and paints.

2. MATERIALS AND METHODS

2.1. Materials. The following ACS grade materials were purchased from Sigma-Aldrich: graphite powders, sulfuric acid (H_2SO_4, 95.0−98.0%), phosphoric acid solution (H_3PO_4, 85 wt %), hydrochloric acid (HCl, 37%), L-ascorbic acid ≥99%, ferric chloride ($FeCl_3$), and sodium carbonate (Na_2CO_3) powder ≥99.5%. Hydrogen peroxide (H_2O_2, 30%), ammonia solution 28−30%, and potassium permanganate ($KMnO_4$) were procured from VWR Canada. Ferrous ammonium sulfate hexahydrate ($H_8FeN_2O_8S_2 \cdot 6H_2O$), barium chloride dihydrate ($BaCl_2 \cdot 2H_2O$), sodium hydroxide (NaOH), acetone >99.5%, and reagent alcohol 94.0−96.0% were purchased from Fisher Scientific.

2.2. Synthesis of TCRGO. The developed two-step reduction protocol, which produces a high quality TCRGO, was applied to investigate its highly conductive properties in binary ceramic nanocomposites.[50] Starting with the improved Hummers' method,[51] 2 g of graphite was added to an acidic mixture of 240 mL of sulfuric acid (H_2SO_4) and 26 mL of phosphoric acid (H_3PO_4) followed by the addition of 12 g of potassium permanganate ($KMnO_4$) in portions while stirring to avoid heat accumulation and guarantee a thorough distribution. It was then left for 3 days. Dropwise additions of hydrogen peroxide (10% H_2O_2) were made until the solution color changed to a yellowish orange, indicating the formation of GO. GO particles were washed by decantation three times with hydrochloric acid (15% HCl). The GO suspension was chemically reduced by adding 0.1 mM L-ascorbic acid solution while stirring at 600 rpm and 80 °C for 4 h. The chemically reduced graphene oxide (CRGO) was collected using a Buchner filtration setup after being washed three times with distilled water (DW) and once with acetone before being dried in a vacuum desiccator overnight. Finally, the dried powders were treated thermally at 200 °C for 4 h under vacuum to produce the TCRGO.

2.3. Synthesis of BF. BF particles were prepared using the coprecipitation method by adding the salt mixture solution at once to an alkaline solution (pH = 13).[52] The alkaline solution was prepared by mixing 1 M sodium hydroxide (NaOH) and 0.1 M sodium carbonate (Na_2CO_3) in the ratio of 4:1 while stirring with an overhead mechanical stirrer with a paddle rod (SS316L/PTFE) at 600 rpm and 110 °C for 2 h. Salt mixtures were prepared with a Fe^{3+}/Ba^{2+} molar ratio of 7:1 by mixing 0.3 M ferric chloride ($FeCl_3$) and 0.04 M barium chloride dihydrate ($BaCl_2 \cdot 2H_2O$). A reddish-brown precipitate appears once the salt mixture is added to the alkaline medium while being stirred at 800 rpm and 95 °C for 2 h. A washing process was done using DW and acetone twice in a centrifuge before the precipitate was collected and dried with a Buchner filtration setup and a vacuum desiccator. The reddish-brown
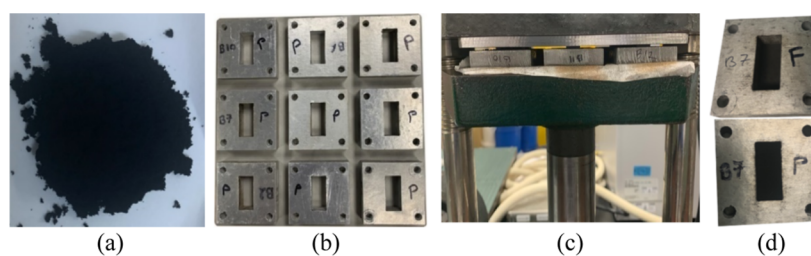
Figure 1. Digital images of the main ceramic nanocomposite powder compaction preparation steps: (a) powder sample, (b) press mold, (c) carver hydraulic press, and (d) WR90 waveguide filled with the sample (photos were captured by the first author).

particles were ground, followed by a calcination process lasting 4 h at 1000 °C to obtain the BF gray nanoparticles.

2.4. Synthesis of MAG. MAG was synthesized by coprecipitating ferrous and ferric solution salts in an alkaline medium.[53] First, 0.5 M alkaline solution was prepared by dissolving sodium hydroxide (NaOH) in DW at a pH of 14. The alkaline solution was stirred at 650 rpm by an overhead mechanical stirrer with a paddle rod (SS316L/PTFE) at 95 °C for 2 h. Then, the salt solution was prepared by mixing ferric chloride ($FeCl_3$) and ferrous ammonium sulfate hexahydrate ($H_8FeN_2O_8S_2 \cdot 6H_2O$) with Fe^{2+}/Fe^{3+} in the ratio of 1:2. The black MAG particles are formed after adding all salt solution to the alkaline medium while stirring at 850 rpm and 95 °C for 1 h. The MAG particles were washed three times with an ammonia solution of 28−30% and then twice with ethanol and acetone by centrifugation. The nanoparticles were grounded after drying using a Buchner filtration setup and a vacuum desiccator.

2.5. Ceramic Nanocomposite Preparation. Ceramic nanocomposite samples were prepared by applying a simple mechanical mixing using a pestle and mortar followed by a powder compaction technique (420 MPa for 1 min) as demonstrated in Figure 1 (see caption for the identification of steps).

To produce 1 g of nanoceramic for the EMI shielding evaluation, different weights of TCRGO were added to the studied metal oxides (i.e., BF and MAG), forming 1, 5, 10, 15, 20, and 25 wt %. The details of the produced samples are summarized in Table 1.

2.6. Characterization. The prepared samples and nanocomposites' morphology was studied with a scanning electron microscope/energy-dispersive X-ray Hitachi TM3030 Plus tabletop microscope operated at 15 kV and a JEOL JEM-

2100F transmission electron microscope operating at 200 kV. The X-ray diffraction (XRD) patterns were recorded using a Bruker D8 ADVANCE X-ray diffractometer equipped with a LYNXEYE linear position-sensitive detector (Bruker AXS, Madison, WI) using a Co Kα source, X-ray wavelength (λ = 0.15418 nm), and 2θ from 5 to 60° with 0.02° per step and a scanning rate of 0.2°/s. The hysteresis loop of the prepared BF and MAG was provided by a vibrating sample magnetometer (VSM) (GMW, Magnet systems, model 3473-70) equipped with a 70 Amp coil pair and a 96 mm coil gap. The observed hysteresis loops were used to determine the saturation magnetization (M_s), remanent magnetization (M_r), and coercivity (Hc). A Jandel four-point probe with a Magnetron m-800 equipment connected to an Agilent B2902A voltage—current source measuring unit was used to measure the sample's electrical conductivity as dry, circular-shaped pellets at room temperature. The mean conductivity was determined by averaging five measurements.[54] The ceramic nanocomposite's Fourier transform infrared (FTIR) spectra were determined using a PerkinElmer Spectrum 65 FTIR spectrometer equipped with an attenuated total reflectance mode (Miracle ATR) with 64 sample/scan spectra and a resolution of 4 from 500 to 4000 cm^{-1}. Raman spectra were evaluated using a WITec Raman spectrometer equipped with a motorized stage alpha300 access microscope. Data were collected using a 532 nm excitation UHTS300S_GREEN_-NIR laser source and 14 mW of power with a 50×: Zeiss Epiplan, and the number of accumulations was 25 for 15 s integration time. The electromagnetic shielding evaluation was carried out by the Keysight PNA-X Network Analyzer model N5247B at the Poly-Grames Research Center using two open-ended waveguides (WR-90) connected with the sample holder (22.86 mm × 10.16 mm) and calibrated using the Thru—Reflect—Line calibration.[55] A hydraulic press was used to compress 1 g at 420 MPa for 1 min, and the thickness was 1 $\pm$ 0.2 mm. The SER, SEA, and SET were calculated over the X-band from 8.2 to 12.4 GHz, and the relative permittivity and permeability were calculated using a measurement model called the "reflection/transmission μ and ε polynomial fit model" via the Keysight N1500A materials measurement software suite.

3. RESULTS AND DISCUSSION

3.1. Morphology. The morphologies of TCRGO, BF, and MAG were studied by transmission electron microscopy (TEM) with a magnification level of 60k, as shown in Figure 2. Figure 2a depicts the tailored two-step reduction protocol's TCRGO thin wrinkled sheets; the red arrows indicate the layer thickness (2.6 $\pm$ 0.2 nm). Figure 2b,c shows the BF and MAG at 20 nm scale, respectively, indicating the success of nanoparticle synthesis. The BF particles are mostly circular

Table 1. Summary of the Prepared TCRGO/Metal-Oxide Ceramic Nanocomposites

sample	TCRGO (g)	TCRGO (wt %)	nanocomposite's nomenclature
BF	0.01	1	1% TCRGO/BF
	0.05	5	5% TCRGO/BF
	0.1	10	10% TCRGO/BF
	0.15	15	15% TCRGO/BF
	0.2	20	20% TCRGO/BF
	0.25	25	25% TCRGO/BF
MAG	0.01	1	1% TCRGO/MAG
	0.05	5	5% TCRGO/MAG
	0.1	10	10% TCRGO/MAG
	0.15	15	15% TCRGO/MAG
	0.2	20	20% TCRGO/MAG
	0.25	25	25% TCRGO/MAG
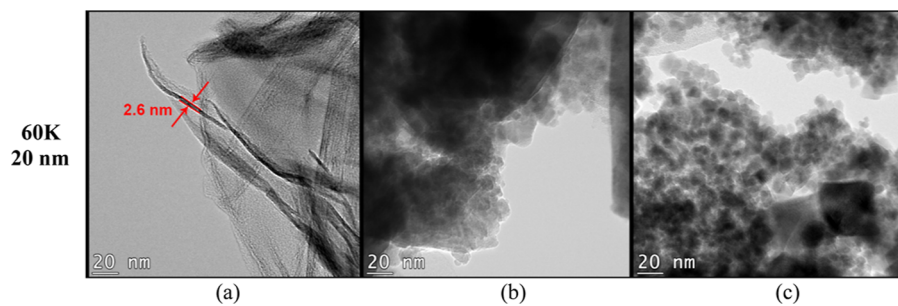
Figure 2. TEM images of individual samples [20 nm]: (a) TCRGO, (b) BF, and (c) MAG.
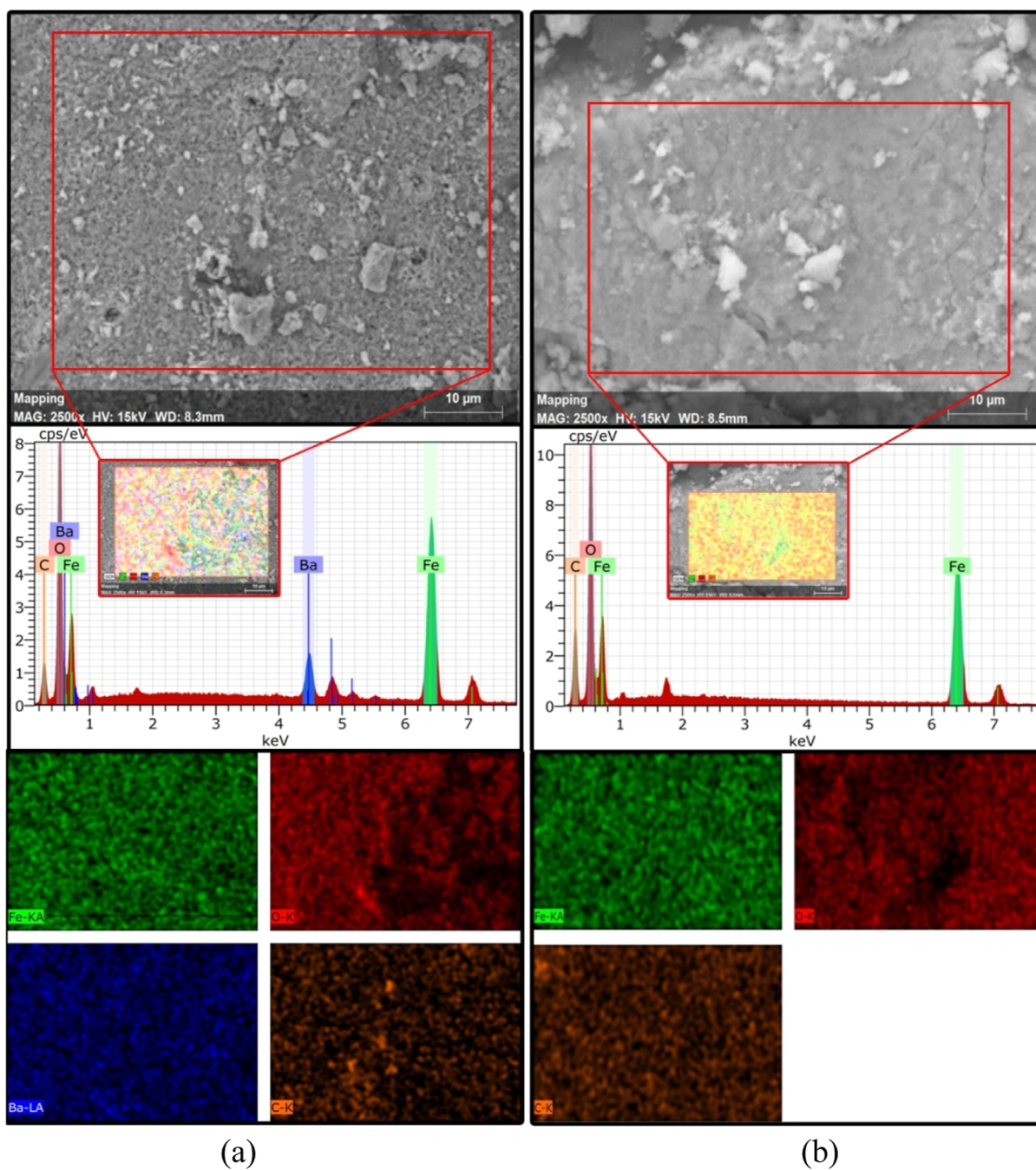
Figure 3. Scanning electron microscopy and EDS images of nanocomposites at 2.5k magnification with mapping: (a) TCRGO/BF nanoceramic sheet and (b) TCRGO/MAG nanoceramic sheet.
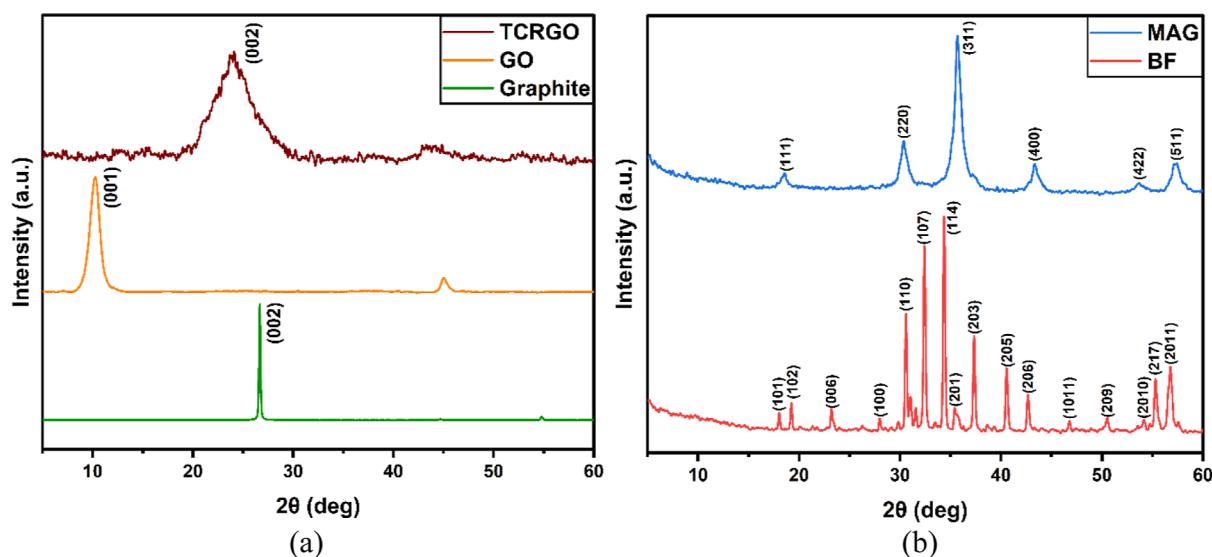
Figure 4. XRD patterns: (a) graphite, GO, and TCRGO and (b) MAG and BF with diffraction peak identification.

(∼8 nm), with the presence of coarse irregular shapes of approximately 220 nm due to the calcination process, while the MAG particles are a blend of circular and rectangular forms (∼6.5 nm). The BF and MAG morphologies agree with the chemical coprecipitation preparation approach.

Moreover, the produced nanoceramic sheets used for the shielding performance evaluation were inspected as a compressed powder by cutting it from the waveguide sample holder after the EMI shielding evaluation to ensure the homogeneity of the formed shielding material (Figure 3). After powder compaction at 420 MPa for 1 min, the ceramic sheets look well distributed and homogeneous, as illustrated in Figure 3a,b, revealing good mixing and validating the nanoceramic sheet preparation method. Energy-dispersive spectroscopy (EDS) indicates the presence of TCRGO by its characteristic carbon peak at ∼0.28 keV. iron and barium are distinguished by two specific peaks. The iron peaks exist at 0.71 and 6.39 keV and the barium peaks at 0.97 and 4.47 keV, while the oxygen peak appears at ∼0.52 keV.

3.2. XRD Characterization. The TCRGO pattern in Figure 4a represents a successful preparation in which the graphite characteristic diffraction peak at $2\theta = 26°$ (002) is converted to $2\theta = 10°$ (001), representing the GO,[56] which disappears upon reduction and forms the TCRGO pattern diffraction peak at $2\theta = 24°$. The synthesized MAG (Fe_3O_4) and BF ($BaFe_{12}O_{19}$) particles were confirmed by their respective peaks shown in the XRD patterns in Figure 4b. The $BaFe_{12}O_{19}$ diffraction peaks were found at $2\theta = 18.03$ (101), 19.24 (102), 23.21 (006), 27.99 (100), 30.59 (110), 32.42 (107), 34.37 (114), 35.43 (201), 37.33 (203), 40.57 (205), 42.68 (206), 46.79 (1011), 50.49 (209), 54.14 (2010), 55.31 (217), and 56.76 (2011).[57] The MAG pattern shows peaks at $2\theta = 18.5$ (111), 30.35 (220), 35.69 (311), 43.31 (400), 53.67 (422), and 57.41 (511).[58] Both patterns agree with the standard XRD pattern COD card number of BF [00-100-8328] and MAG [00-900-5815].

The nanoceramics (i.e., TCRGO/MAG and TCRGO/BF) provide the same characteristic peaks of both metal oxides, and with the increase of TCRGO loading in the nanocomposite, a small broad peak at $2\theta = 24°$ appears. Figure 5 elucidates the 25% TCRGO in both BF and MAG nanoceramic sheets, where
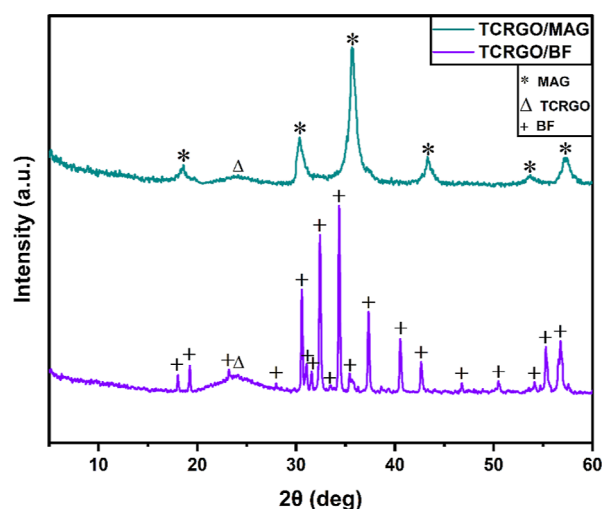
Figure 5. XRD patterns of 25% TCRGO/BF and 25% TCRGO/MAG nanoceramics.

the BF diffraction peaks are noted with (+), MAG with (*), and the TCRGO broad diffraction peak with (Δ). By applying the Debye−Scherrer equation, the average crystallite size can be estimated. The crystallite size of 25% TCRGO/BF was 346 Å, while that of 25% TCRGO/MAG was 77 Å. The expected advantage of BF with TCRGO having a larger crystallite size agrees with the fact that larger crystallite sizes will have a significant impact on enhancing the nanocomposite's conductive properties, interfacial polarization, charge transfer, and shielding effectiveness.[59]

3.3. VSM. The magnetic properties of BF and MAG nanoparticles were evaluated using the VSM, and the saturation magnetization (M_s), coercivity (Hc), and retentivity (M_r) values were determined from the obtained hysteresis loop shown in Figure 6. The BF nanoparticles have a M_s equal to 57 (emu/g), and the Hc and M_r are 46 (Oe) and 13 (emu/g), respectively. The MAG nanoparticle M_s was 49 (emu/g), while its Hc was 11 (Oe) and its M_r was equal to 1 (emu/g).

The hysteresis loop of the nanoparticles implies a superparamagnetic behavior, which is common with the nanoscale preparation of magnetic materials.[60,61] The BF has a higher M_s
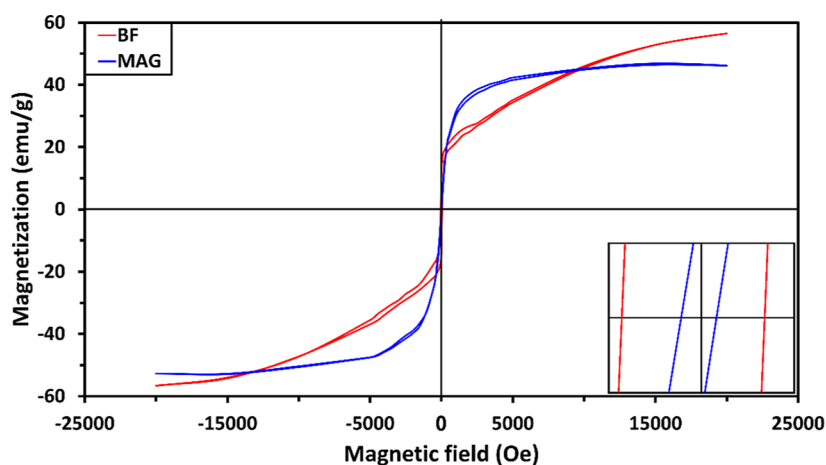
Figure 6. BF and MAG nanoparticle hysteresis loop. The inset demonstrates the coercivity field intensity (Hc) of BF as a hard magnet and MAG as a soft magnet.

than the MAG by 124%, yet both offer high magnetic properties that make them a suitable candidate in conjunction with TCRGO to produce the nanoceramic composite with high expectations for a high EMI shielding performance.

3.4. Electrical Conductivity. Both magnets have saturation magnetization of 57 and 46 emu/g for BF and MAG, respectively, which indicates their high magnetic properties, making them capable to deal with the magnetic parameter of EM waves. The low electrical conductivity blocks its absorption ability, which can then be regulated by adding a highly conductive material to enhance the impedance matching and promote its absorption of EM radiation.[62] The developed two-step protocol offers high-quality TCRGO with a high conductivity of 2.14×10^3 (S/m). It is worth noting that determining the electrical conductivity of graphene as a compressed powder is a difficult task because they are anisometric particles with a high surface area; as a result, a high number of particle contacts affect the bulk conductivity and lowers its values, rendering it incomparable with the electrical conductivity of their composite.[50,54] Pure BF and MAG have a conductivity of 15 ± 3 and 19 ± 3 (S/m), respectively. These values dramatically increase with the addition of TCRGO above 10 wt %.

Figure 7 shows that both magnets were similar up to 10 wt %, at which point the abrupt increase in the electrical conductivity was remarkable up to 25 wt %. BF has the advantage of a large crystallite size, which promotes the
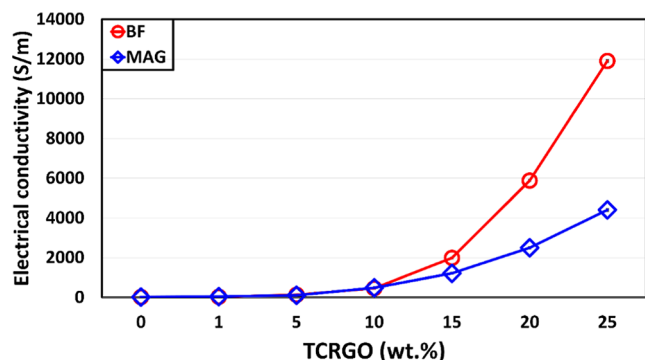
Figure 7. Electrical conductivity of BF and MAG at different TCRGO weight-loading percentages.

interfacial polarization, charge transfer, and nanoceramic composite conductive properties and surpasses the 25 wt % TCRGO/MAG by 270%, scoring 11.9×10^3 (S/m).

3.5. FTIR Spectroscopy Analysis. FTIR spectra of BF and MAG nanocomposites are shown in Figure 8a,b, respectively. The TCRGO functional groups are clarified with a black line presenting the vibrational stretching of C=O (νC=O) at 1720 cm^{-1}, vibrational stretching of C=C (νC=C) at 1570 cm^{-1}, and vibrational stretching at 1220 cm^{-1} of C–O (νC–O) epoxy groups.[63] BF presents the vibrational stretching peak of (Fe–O) at 598 cm^{-1}, while the (–OH) groups are absent due to the evolution of gaseous products during the calcination process. On the other hand, MAG exhibits vibrational bands at (Fe–O) stretching peaks of 570 and 630 cm^{-1} with the (–OH) bending identified by the peaks at 3390, 1642, 1540, and 1340 cm^{-1}.[9,64] The presence of metal oxide and TCRGO peaks gives an indication of the successful mixing procedures of the final product.

3.6. Raman Spectroscopy Analysis. Raman spectroscopy is an effective, nondestructive tool to observe carbonaceous materials. It can also detect the presence of various metal-oxide phases in BF and MAG. Figure 9 shows the TCRGO spectrum with its characteristic D and G bands at 1600 and 1359 cm^{-1}. The G band rises due to the relative vibrational motion of sp^2-hybridized carbon atoms (graphitic lattice structure). The presence of the D band indicates the presence of a defect or disorder.[65] Furthermore, the ratio of the D and G bands indicates the presence of defects in graphene sheets (a high ratio value indicates a high level of disorder).[66] The I_D/I_G ratio was applied using the peak-to-peak height ratio, and it is expected to increase in graphene composite materials since it reflects the estimated degree of graphitization.[67] The TCRGO has an I_D/I_G ratio equal to 0.88. The BF spectra shows a high intense Raman shift located at 186, 343, 418, 474, 535, 620, and 691 cm^{-1}.[9] The MAG phase is characterized by four peaks at 194, 351, 508, and 691 cm^{-1}.[68] The Raman spectra of both BF and MAG samples confirm the absence of the hematite (Fe$_2$O$_3$) phase and indicate the success of sample preparation.[69]

Furthermore, all prepared ceramic nanocomposites confirm the same trend as the combination between the typical peaks of each metal-oxide type with lower intensities and significant and dominant TCRGO bands (i.e., D and G). The I_D/I_G ratios for both samples increase to ~1 as the D peak increases due to
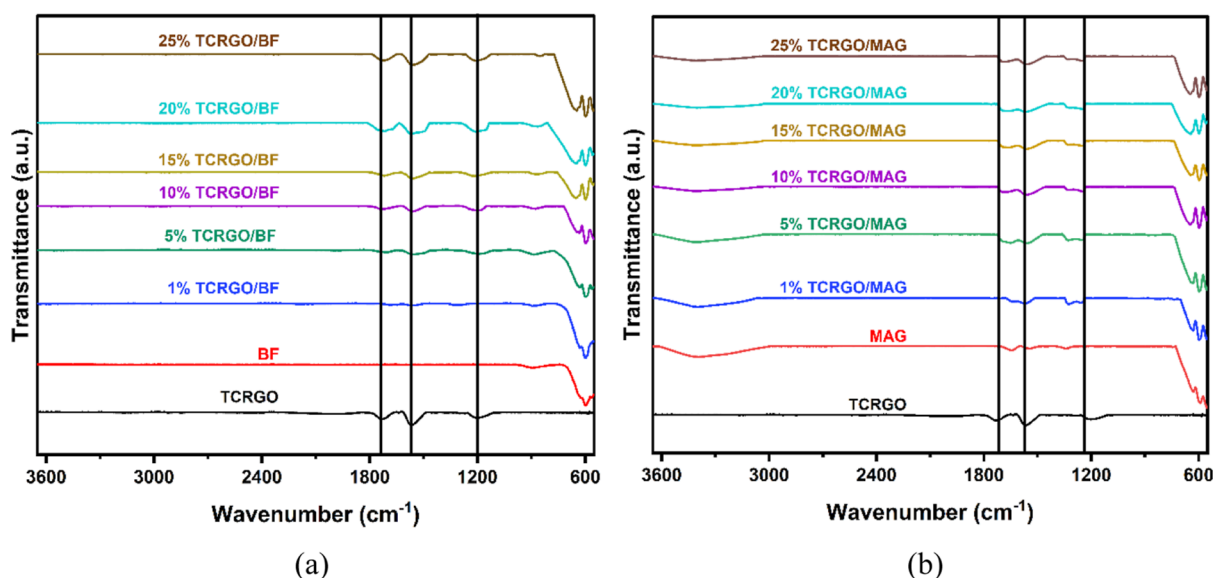
Figure 8. FTIR spectra of (a) TCRGO/BF and (b) TCRGO/MAG nanocomposites; the black lines show the TCRGO peaks.
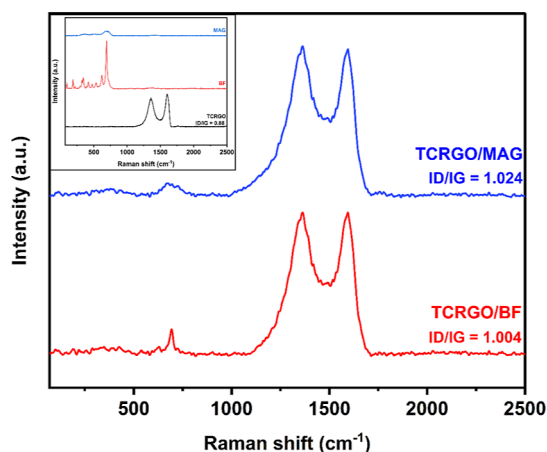
Figure 9. Raman spectra of TCRGO/BF and TCRGO/MAG with I_D/I_G ratio identification. The inset shows the Raman spectra of pure TCRGO, BF, and MAG.

the presence of BF and MAG, which are common in graphene-based composites.

3.7. Electromagnetic Measurements. The incorporation of conductive material with good magnetic material is necessary to manage the magnetic and dielectric losses inside the shield agent and alter the ceramic sheet's overall performance, hence improving the total shielding performance.[70,71] The shielding performance was evaluated by collecting the scattering parameters (S-params) using the VNA transmission waveguide method. The SE of a shield in an electromagnetic environment represents its ability to dissipate or attenuate the electromagnetic field. The coefficients of absorption (A), reflection (R), and transmission (T) can be determined by evaluating the material's response to the field using eqs 1−3. These coefficients provide insight into the material's performance and its capacity to absorb, reflect, or transmit the electromagnetic energy.

$$T = |S_{12}|^2 = |S_{21}|^2 \tag{1}$$

$$R = |S_{11}|^2 = |S_{22}|^2 \tag{2}$$

$$A = 1 - R - T \tag{3}$$

The transmission of electromagnetic waves through a shield leads to three distinct mechanisms of attenuation, namely, reflection loss (SER), absorption loss (SEA), and multiple reflection loss (SEM). These mechanisms can be quantified using the following formulas 4−6[72,73]

$$SER = -10 \, \log(1 - R) \tag{4}$$

$$SEA = -10 \, \log(T/1 - R) \tag{5}$$

$$SET = SEA + SER + SEM \tag{6}$$

For total shielding efficiency (SET) values above 10 dB, the multiple reflection loss (SEM) can be considered negligible.[74] EMI shielding materials with a SET greater than 50 dB correspond to an effective shielding of 99.9% of the incident electromagnetic waves, resulting from a combination of absorption and reflection capacities.[75]

Table 2 clarifies the individual shielding performance of each material. The TCRGO provides 37 dB SET based on its high

Table 2. Averaged SET, SEA, and SER Values of BF, MAG, and TCRGO over the X-Band from 8.2 to 12.4 GHz, with Standard Deviations

sample	SER (dB)	SEA (dB)	SET (dB)
BF	4 ± 0.4	1 ± 0.4	5 ± 0.5
MAG	3 ± 0.2	3 ± 0.1	6 ± 0.3
TCRGO	8 ± 0.6	29 ± 0.8	37 ± 0.3

dielectric loss, with SEA equal to 29 dB. The results indicate that the TCRGO can provide a high level of shielding performance for magnetic ceramics, which suffer from poor conductivity.

Both BF and MAG, as pure nanoceramic shielding materials, have low SET values based mainly on their reflection efficiency, as demonstrated in Table 2. This observation agrees with the literature and indicates the urge to combine them with a highly conductive material to enhance their SET and their absorption capability as a response to commercial demands. Still, the formation of a ceramic nanocomposite is not favored
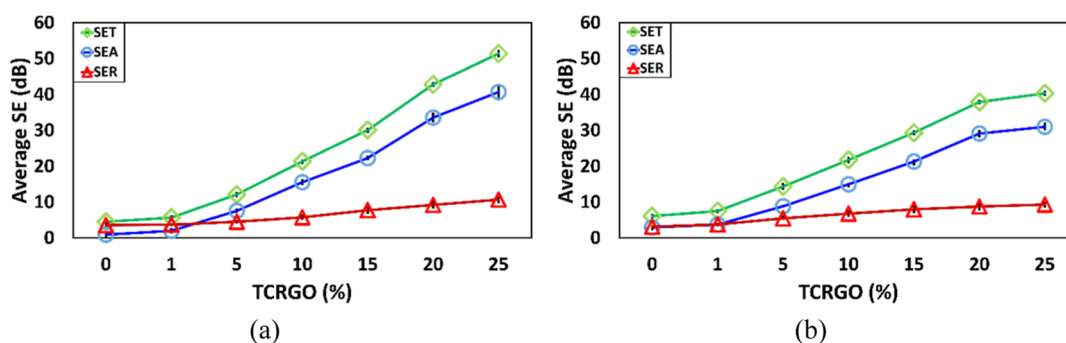
Figure 10. Averaged shielding effectiveness over the X-band: (a) TCRGO/BF nanocomposites. (b) TCRGO/MAG nanocomposites, The error bars represent standard deviations.
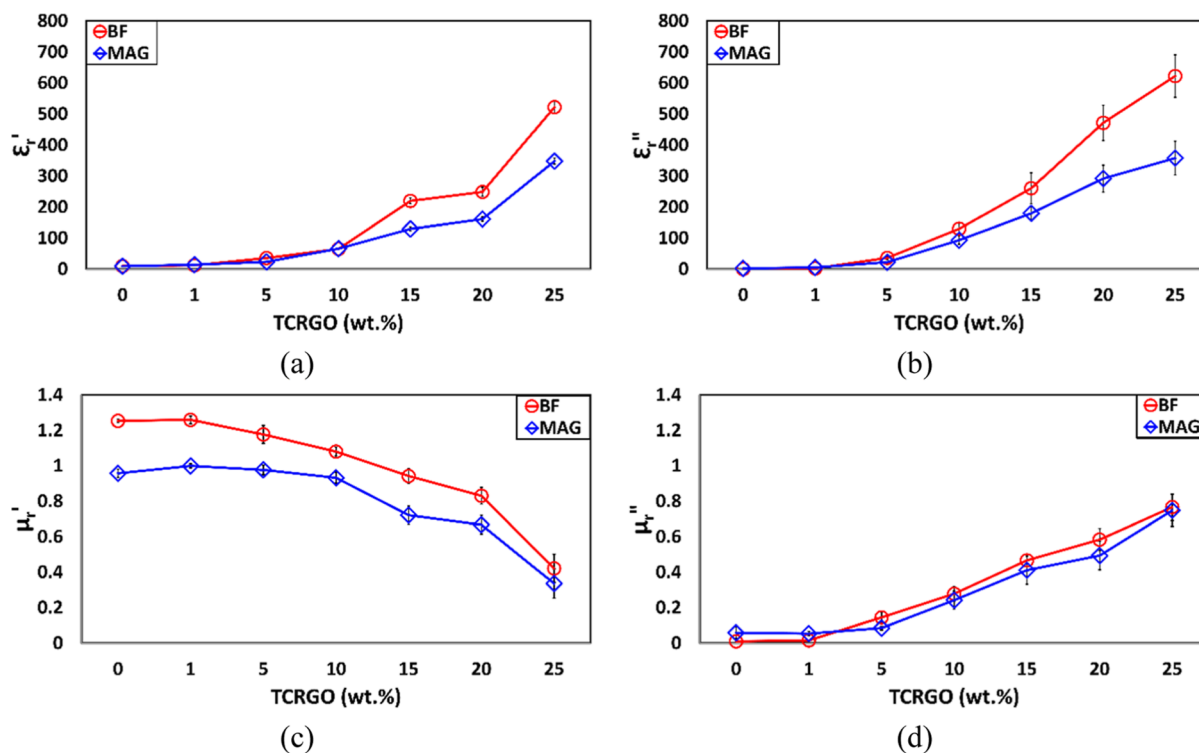
Figure 11. Averaged relative permittivity and permeability over the frequency range 8.2−12.4 GHz of TCRGO/BF and TCRGO/MAG ceramic nanocomposite sheets with different TCRGO amounts: (a) Relative permittivity real part (ε_r'), (b) relative permittivity imaginary part (ε_r''), (c) relative permeability real part (μ_r'), and (d) relative permeability imaginary part (μ_r''). The error bars represent standard deviations.

since they suffer from the low absorption efficiency where the SET was mainly based on the reflection of incident waves. Table 2 summarizes the SET, SEA, SER, and conductivity of the evaluated individual materials.

Figure 10a depicts the significant impact of applying TCRGO on dielectric losses and enhancing the BF absorption abilities. Due to the synergism of both materials, the SEA begins to improve linearly from 1 to 25% TCRGO, indicating an increase in dielectric losses. Additionally, the SER values increase moderately, enhancing the SET. The SET of the 25 wt % TCRGO/BF composite was found to be 52 dB, which is a 10-fold increase compared to the individual BF. The absorption loss (SEA) was measured to be 41 dB, while the reflection loss (SER) was 11 dB. The absorption of the ceramic nanocomposite increased 40 times more than the pure BF ceramic sheet. According to Figure 10b, the addition of TCRGO did not result in a noticeable change in the shielding parameters of MAG at 1%. However, from 5 to 25%, the SEA

values significantly increase due to the consistent arrangement of minute nanoparticles, which contributes to the enhancement of wave absorption performance, and the SER values slightly increase, promoting the SET. A comparable examination was conducted with the 25 wt % TCRGO/MAG composite. The absorption of this composite was found to be 25 times greater than that of the pure MAG ceramic sheet, with a total shielding effectiveness (SET) of 40 dB, an absorption loss (SEA) of 31 dB, and a reflection loss (SER) of 9 dB.

The TCRGO/BF shielding improvement reflects the synergism between BF as a hard magnet due to its high saturation magnetization and magnetic anisotropy and the highly conductive TCRGO particles, which promote the interfacial polarization and charge transfer within the nanoceramic composite, which surpasses the MAG shielding values.
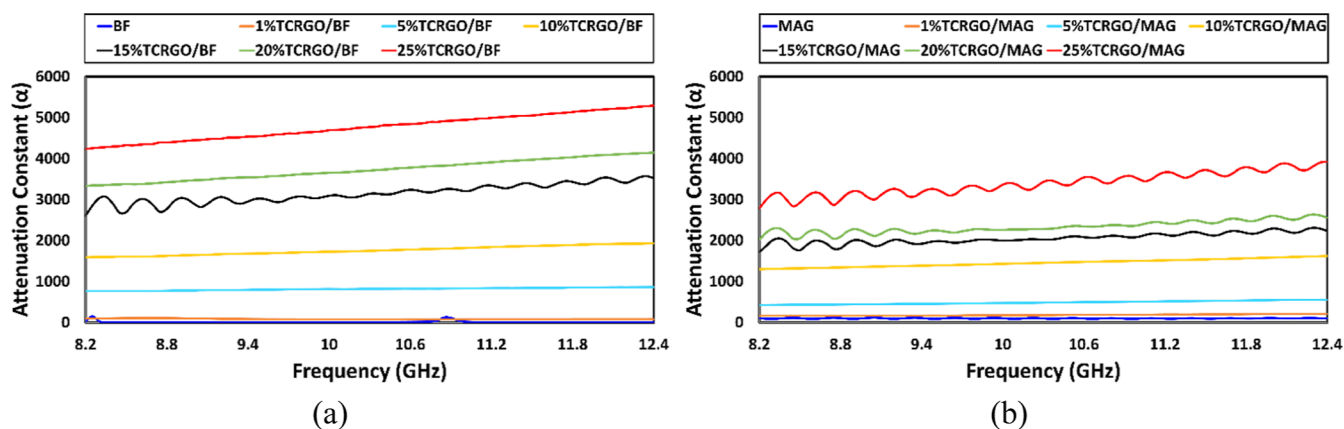
Figure 12. Attenuation constant (α): (a) TCRGO/BF and (b) TCRGO/MAG ceramic nanocomposites over the X-band (frequency range: 8.2–12.4 GHz).

The relative permittivity (ε_r) and permeability (μ_r) of the material are linked to the EMI shielding (SER, SEA, and SET) by the following equations[72,76]

$$SER \approx 10 \ \log[\sigma_{ac}/16\omega\varepsilon_0\mu_r] \tag{7}$$

$$SEA = 20[t/\delta]\log e = 20t\sqrt{\omega\sigma_{ac}\mu_r/2} \tag{8}$$

$$SET = 10 \ \log[\sigma_{ac}/16\omega\varepsilon_0\mu_r] + 20t\sqrt{\omega\sigma_{ac}\mu_r/2} \tag{9}$$

The reflection loss (SER) and absorption loss (SEA) of a shielding material are dependent on various factors such as the dielectric properties of the material, the angular frequency (ω), the skin depth (δ), the permitivity of free space (ε_0), and the material's thickness (t). The equation for the SER indicates that it is inversely proportional to the magnetic permeability (μ_r) and directly proportional to the electrical conductivity (σ_{ac}). Conversely, the SEA is proportional to the square root of both σ_{ac} and μ_r.

Figure 11a shows the real relative permittivity part (ε_r'), which reflects the energy storage of the ceramic nanocomposites. Both TCRGO/BF and TCRGO/MAG show a similar trend. At 15 wt %, the TCRGO/BF energy storage values surpass those of the TCRGO/MAG and score an increase of 150% at 25 wt %. The imaginary part, which corresponds to the energy losses (ε_r''), is shown in Figure 11b. A similar trend was observed for both nanoceramics; they increased as the TCRGO amounts increased, demonstrating the effect of the TCRGO addition to the ceramic nanocomposite. In addition, the TCRGO/BF ceramic sheet provides higher energy losses over 10 wt % TCRGO.

At 25 wt %, the energy loss of TCRGO/BF is double that of TCRGO/MAG, indicating that the synergism between the developed TCRGO and the large crystallite size of BF nanoparticles provides a high ability to absorb the EMI waves due to the interfacial polarization and charge transfer, which promote the electrical conductivity of the ceramic nanocomposite sheet. Figure 11c,d shows the relative permeability values of the real part (μ_r') representing the magnetic storage and the imaginary part (μ_r'') denoting the magnetic loss, respectively. Both BF and MAG are magnetic materials, and there is no remarkable difference between their relative permeabilities. μ_r' decreases with the decrease of BF and MAG amounts in the samples. μ_r'' increases even with the

increase of the nonmagnetic TCRGO's weight load percentage, which suggests the impact of the tailored TCRGO in conjunction with the dispersed magnetic nanoparticles of the ceramic nanocomposite by developing the interfacial magnetic domain and enhancing the magnetic loss of the nanocomposite.[77] The results from Figure 11b,d indicate that the electromagnetic absorbance capabilities of the materials are highly correlated with the dielectric and magnetic properties, particularly the imaginary components of permittivity and permeability.[78] The complex permittivity and permeability values reveal the dependence of the absorption performance on the presence of TCRGO, as a high dielectric material, and its synergistic effect with the BF and MAG nanoparticles, as magnetic materials, which reflects the impedance matching enhancement properties of the final ceramic nanocomposite sheet.

Attenuation is a measure of the loss of energy in a wave as it passes through a material or medium. The attenuation constant is represented by the symbol (α) and expressed in decibels (dB). It is used to evaluate the integral loss ability, as expressed in eq 10.[79]

$$\alpha = \frac{\sqrt{2}\,\pi f}{c}\left(\sqrt{(\mu''\varepsilon'' - \mu'\varepsilon')} + \sqrt{(\mu''\varepsilon'' - \mu'\varepsilon')^2 + (\mu'\varepsilon'' + \mu''\varepsilon')^2}\right) \tag{10}$$

The testing frequency is represented by f (in Hz), and c represents the speed of light in a vacuum (in m/s).

Figure 12 shows the effect of TCRGO loading on the attenuation constant (α). As the TCRGO loading increases, the attenuation constant also increases over the X-band in the range of 8.2–12.4 GHz, indicating high levels of loss.

The 25 wt % TCRGO/BF and TCRGO/MAG ceramic nanocomposites exhibit improved microwave absorption performance due to the effective dissipation of electromagnetic waves that enter the interiors of these absorbers, with the 25 wt % TCRGO/BF showing particularly advantageous performance, surpassing other samples.[80,81] A high attenuation value demonstrates a synergistic enhancement of dielectric and magnetic energy loss, leading to a more effective absorption of the wave by the ceramic nanocomposite.[82] Additionally, the effective absorption percentage, denoted as A_{eff}, is a metric used to assess the efficiency of an EMI shielding material in absorbing EMI. It represents the fraction of incident EMI power that is absorbed by the material and is expressed as a percentage by applying the following formula[83]

Table 3. Average Effective Absorption Percentage (A_{eff}) of TCRGO/BF and TCRGO/MAG Ceramic Nanocomposites over the X-Band from 8.2 to 12.4 GHz

sample	TCRGO/BF						TCRGO/MAG					
	1%	5%	10%	15%	20%	25%	1%	5%	10%	15%	20%	25%
A_{eff} (%)	36.58	82.61	97.21	99.41	99.96	99.99	57.85	86.97	96.83	99.26	99.88	99.92

$$A_{eff} = (1 - T - R)/(1 - R) \times 100 \tag{11}$$

Table 3 displays the results of the effective absorption for the ceramic samples that were analyzed. The sample composed of 25 wt % TCRGO/BF achieved an effective absorption of 99.99%, while the sample with 25 wt % TCRGO/MAG demonstrated an effective absorption of 99.92%. These results indicate a high capability of the samples in absorbing electromagnetic wave.

Therefore, the magnetic and dielectric loss tangents are critical factors that influence the efficiency of absorption in an absorber. A high loss tangent implies a higher capability to transform electromagnetic waves into alternative forms of energy. The dielectric and magnetic tangential losses for the 25 wt % TCRGO/BF and TCRGO/MAG can be evaluated from the detected relative permittivity and permeability values according to eqs 12 and 13, respectively.

$$\tan \delta_e = \frac{\varepsilon_r''}{\varepsilon_r'} \tag{12}$$

$$\tan \delta_m = \frac{\mu_r''}{\mu_r'} \tag{13}$$

Figure 13 demonstrates the loss tangent behavior of the 25 wt % ceramic nanocomposites in the frequency range of 8.2–
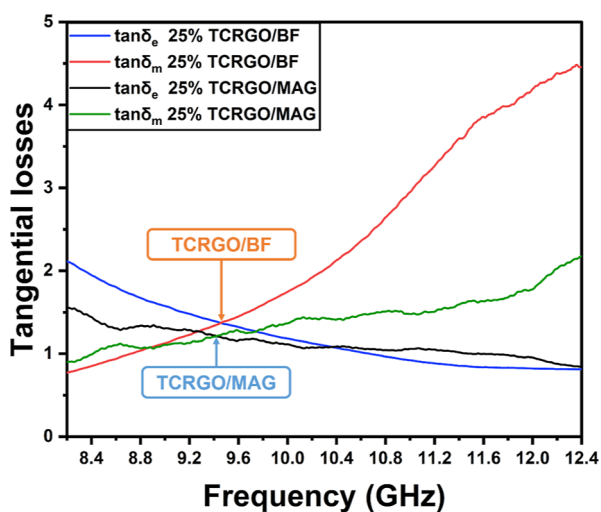
Figure 13. Dielectric and magnetic loss tangent of 25 wt % TCRGO/BF and TCRGO/MAG ceramic nanocomposites in the frequency range of 8.2–12.4 GHz. The orange and blue arrows indicate the dielectric and magnetic loss intersection.

12.4 GHz. The dielectric loss tangent ($\tan \delta_e$) declines for both samples at high frequencies, with an advantage for BF between 8.2 and 10.4 GHz.

The magnetic loss tangent ($\tan \delta_m$) increases dramatically as the frequency increases. BF provides a higher $\tan \delta_m$ than MAG, which starts at 8.8 GHz (intersection between the red and green curves) and dramatically increases at 10.4 GHz. tan

δ_e and $\tan \delta_m$ demonstrate a counteractive trend when the frequency is increased. Consequently, they intersect at a point, marked by the blue and orange arrows for TCRGO/BF and TCRGO/MAG, respectively. This suggests the ceramic nanocomposite's minimal loss value. The 25 wt % TCRGO/BF minimum loss value equals 1.4 at 9.5 GHz, and the 25 wt % TCRGO/MAG is 1.2 at 9.4 GHz. Furthermore, this intersection represents $\tan \delta_m = \tan \delta_e$ where both losses effectively enhance the microwave absorption capacity. This finding is consistent with the fact that absorbing materials are frequency-dependent, and it indicates that both losses contribute to energy consumption and proposes a complementary loss tangent effect that helps to improve EMI shielding via the absorption mechanism.[78,84]

The high SEA of the 25 wt % TCRGO/BF sample indicates the effective synergies from the two losses, which promote the ceramic nanocomposite's absorption performance. This integration improves the impedance matching and enables the penetration of the incident EM wave through the sample. The significant role of $\tan \delta_m$ along with $\tan \delta_e$ can provide an advanced EMI shielding absorber.

The relationship of the material thickness on the SEA and SET at a constant power is directly proportional, which coincides with the shielding theory. The effect of varying levels of incoming wave power at varying thicknesses remains intriguing as we try to understand the material's shielding mechanism based on its reflection and absorption properties. Based on the previous observations, the optimal sample (i.e., 25% TCRGO/BF) was investigated further to determine the influence of different thicknesses and levels of incident electromagnetic wave power. As shown in Figure 14, three different thicknesses of 1, 2, and 5 mm were prepared and evaluated at various levels of power of 0.001, 0.01, 0.3, 100, and 1000 mW.

The SER of the nanocomposite followed a similar profile across all investigated thicknesses; it increased moderately with higher incoming power starting at 0.3 mW incident power, as shown in Figure 14a–c. The core difference for the SET is related to the nanocomposite's absorption ability. The SEA decreases gradually for both 1 and 2 mm until it reaches 100 mW and then remains relatively stable. This suggests that for low incident powers, the energy can be completely absorbed inside the materials. By increasing the incoming power, the energy begins to penetrate, while the materials absorb and reflect the radiation relative to their amounts and thicknesses, offering its SET. As a result of this behavior, the nanocomposite maintains its total shielding performance at high levels of incident electromagnetic wave power of 47 and 67 dB, respectively.

The 5 mm thickness shown in Figure 14c provides a consistent SEA when subjected to diverse power levels, even at high values, while the SER trend remains identical to other thicknesses; as a result, the SET is quite enhanced, offering 98 dB. This absorption ability was obtained because of the substantial dielectric losses generated by the quantity introduced to obtain a 5 mm ceramic sheet. The observed
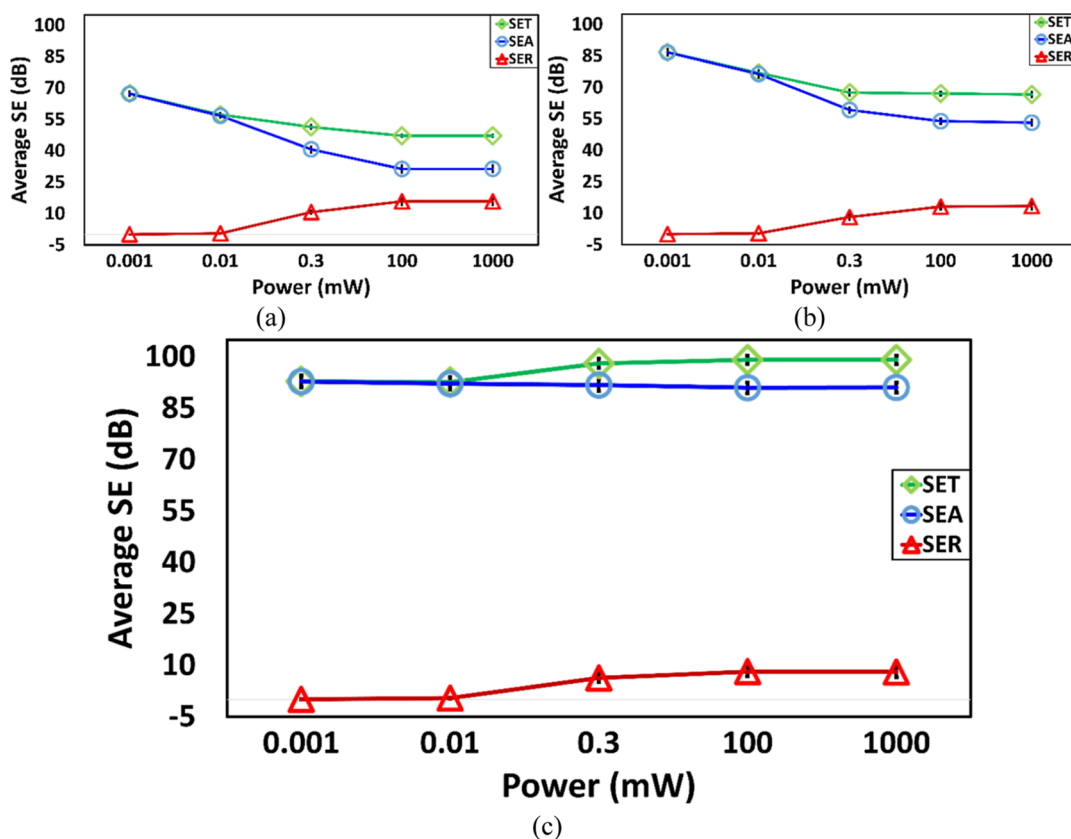
Figure 14. Effect of electromagnetic wave power on the 25 wt % TCRGO/BF nanocomposite at different thicknesses: (a) 1, (b) 2, and (c) 5 mm. The error bars represent standard deviations.

Table 4. Metal-Oxide/Carbon-Based Nanocomposite EMI Shielding Systems

#	the composite	SET (dB)	frequency (GHz)	preparation method	sample thickness (mm)	refs
	$BaFe_{12}O_{19}$/RGO	32	12.4−18	ball milling	3	9
1	RGO/Fe_3O_4 hybrid-modified carbon foams	63.5	8.2−12.4	coprecipitation method	3	15
2	$BaFe_{12}O_{19}$/MWCNT/PANI	40	8−12	in situ polymerization	not specified	30
3	carbon foam (CF)	35	8.2−12.4	self-foaming method	2	74
4	PANI/BF/EG	37	8.2−12.4	insitu polymerization	not specified	85
5	PVDF/MWCNT	35	8.2−12.4	solution casting	5	86
6	PVDF/CNT	20.3	8.2−12.4	melt-mixed/compression molded	1.1	87
7	RGO/Fe_3O_4/BST	48	8.2−12	chemical oxidative polymerization	2.5	88
8	$Ni_{0.5}Co_{0.5}Fe_2O_4$/RGO	36.3	12.4−18	insitu synthesis	2	89
9	Fe_3O_4/GO/carbon fibers	46.3	8.2−12.4	coprecipitation/magnetic encapsulation	not specified	90
10	PVDF/graphene	22.6	18−26	solvent casting/compression-molding	0.1	91
11	ABS/CNT	50	8.2−12.4	solution processing	1.1	92
12	RGO/$MnFe_2O_4$/MWCNTs/PVDF	38	2−18	hydrothermal method	5.5	93
14	TCRGO/BF	52	8.2−12.4	powder compaction	1	this work
15	TCRGO/MAG	40	8.2−12.4	powder compaction	1	this work

findings deliver an optimization when high incident power is an issue. At 1000 mW incident power, the 5 mm thickness of a 25 wt % TCRGO/BF nanoceramic sheet achieves 99 dB SET; the SEA is 91 dB, and the SER is 8 dB.

Based on the previous results, BF as a hard magnet has a high permeability complex mechanism. In addition, its large crystallite size promotes interfacial polarization and charge transfer when coupled with TCRGO, which leads to the enhancement of nanocomposite conductive properties and reflects on its dielectric and magnetic losses. The BF/TCRGO synergistic effect offers a high-performance shielding nano-composite material that can be applied as a potential candidate in EMI shielding paints, foams, polymeric resins, and adhesives. Table 4 demonstrates some reported metal-oxide/carbon-based nanocomposits systems.

4. CONCLUSIONS

The addition of TCRGO as a high dielectric loss material in binary nanocomposites comprising BF with its noticeable magnetic characteristics adjusts the nanocomposite's impe-dance and hence its absorption capabilities. As a result, the

shielding performance outperforms its separate equivalents, highlighting the synergistic impact within the nanocomposite.

This study explores the effect of two different magnet types (soft and hard), synthesized through a coprecipitation technique in conjunction with different TCRGO loads to produce a binary nanocomposite via traditional mechanical mixing. The shielding performance of 1 mm thick samples was evaluated, and superior shielding values were obtained at 25% TCRGO. The SET of BF surpassed that of MAG by 130%. The observed SEA was 41 dB and SER was 11 dB, resulting in a SET of 52 dB, which is 10 times greater than that of individual BF. It indicates the effective impact of improving the absorption of ceramic nanocomposite sheets due to the dielectric and magnetic tangential losses' complementary effect. Furthermore, the study investigates the effect of different levels of incident electromagnetic wave power at various material thicknesses on its shielding behavior in terms of reflection and absorption. The 5 mm thickness provides stable and outstanding shielding performance due to its ability to maintain the SEA values in front of the increased power. It has SEA, SER, and SET measurements of 91, 8, and 99 dB, respectively.

The binary ceramic nanocomposite based on BF and TCRGO presented in this work solves the disadvantages of single materials by providing both high dielectric and magnetic losses, enhancing its absorption capability while providing a superior shielding performance. The results surpass the shielding limitations for commercial demands, making these ceramic nanocomposites a target for further development in the field of EMI shielding materials, which encompasses a wide range of civil and military applications.

■ AUTHOR INFORMATION

Corresponding Author

Jamal Chaouki − *Chemical Engineering Department, Polytechnique Montréal, Montréal, Quebec H3T 1J4, Canada;* ⊙ orcid.org/0000-0001-8353-6924; Email: jamal.chaouki@polymtl.ca

Authors

Ramy Sadek − *Chemical Engineering Department, Polytechnique Montréal, Montréal, Quebec H3T 1J4, Canada;* ⊙ orcid.org/0000-0001-9710-0566

Mohammad S. Sharawi − *Poly-Grames Research Center, Electrical Engineering Department, Polytechnique Montréal, Montréal, Quebec H3T 1J4, Canada*

Charles Dubois − *Chemical Engineering Department, Polytechnique Montréal, Montréal, Quebec H3T 1J4, Canada*

Hesham Tantawy − *Chemical Engineering Department, Military Technical College, Cairo 11766, Egypt;* ⊙ orcid.org/0000-0001-5481-7049

Complete contact information is available at:
https://pubs.acs.org/10.1021/acsomega.2c08168

Notes

■ ACKNOWLEDGMENTS

■ REFERENCES

(1) Redlarski, G.; Lewczuk, B.; Żak, A.; Koncicki, A.; Krawczuk, M.; Piechocki, J.; Jakubiuk, K.; Tojza, P.; Jaworski, J.; Ambroziak, D.; et al. The Influence of Electromagnetic Pollution on Living Organisms: Historical Trends and Forecasting Changes. *BioMed Res. Int.* **2015**, *2015*, 1.

(2) Perrin, A.; Souques, M. *Electromagnetic Fields, Environment and Health*, 1st ed.; Springer: Paris, 2013; pp 1−9.

(3) Majid, R. J. EMI Effects in Flight Control Systems and Their Mitigations. *Handbook of Aerospace Electromagnetic Compatibility-Chapter 10: EMI effects in flight control systems and their mitigations*; Wiley, 2018; pp 537−602.

(4) Adebayo, L. L.; Soleimani, H.; Yahya, N.; Abbas, Z.; Wahaab, F. A.; Ayinla, R. T.; Ali, H. Recent advances in the development OF Fe3O4-BASED microwave absorbing materials. *Ceram. Int.* **2020**, *46*, 1249−1268.

(5) Shen, S.-Y.; Zheng, H.; Zheng, P.; Wu, Q.; Deng, J.-X.; Ying, Z.-H.; Zheng, L. Microstructure, magnetic properties of hexagonal barium ferrite powder based on calcination temperature and holding time. *Rare Met.* **2021**, *40*, 981−986.

(6) Nikmanesh, H.; Moradi, M.; Bordbar, G. H.; Shams Alam, R. S. Effect of multi dopant barium hexaferrite nanoparticles on the structural, magnetic, and X-Ku bands microwave absorption properties. *J. Alloys Compd.* **2017**, *708*, 99−107.

(7) Liu, X.; Wang, J.; Ding, J.; Chen, M.; Shen, Z. The effects of mechanical activation in synthesizing ultrafine barium ferrite powders from co-precipitated precursors. *J. Mater. Chem.* **2000**, *10*, 1745−1749.

(8) Li, Y.; Yi, R.; Yan, A.; Deng, L.; Zhou, K.; Liu, X. Facile synthesis and properties of ZnFe2O4 and ZnFe2O4/polypyrrole core-shell nanoparticles. *Solid State Sci.* **2009**, *11*, 1319−1324.

(9) Verma, M.; Singh, A. P.; Sambyal, P.; Singh, B. P.; Dhawan, S.; Choudhary, V. Barium ferrite decorated reduced graphene oxide nanocomposite for effective electromagnetic interference shielding. *Phys. Chem. Chem. Phys.* **2015**, *17*, 1610−1618.

(10) Sharif, F.; Arjmand, M.; Moud, A. A.; Sundararaj, U.; Roberts, E. P. Segregated Hybrid Poly(methyl methacrylate)/Graphene/Magnetite Nanocomposites for Electromagnetic Interference Shielding. *ACS Appl. Mater. Interfaces* **2017**, *9*, 14171−14179.

(11) Uma Varun, V.; Rajesh Kumar, B.; Etika, K. C. Hybrid polymer nanocomposites as EMI shielding materials in the X-band. *Mater. Today: Proc.* **2020**, *28*, 796−798.

(12) Ting, T. H. Synthesis, characterization of Fe3O4/polymer composites with stealth capabilities. *Results Phys.* **2020**, *16*, 102975.

(13) Wu, N.; Liu, C.; Xu, D.; Liu, J.; Liu, W.; Shao, Q.; Guo, Z. Enhanced electromagnetic wave absorption of three-dimensional porous Fe3O4/C composite flowers. *ACS Sustainable Chem. Eng.* **2018**, *6*, 12471−12480.

(14) Wang, Z.; Wu, L.; Zhou, J.; Shen, B.; Jiang, Z. Enhanced microwave absorption of Fe3O4 nanocrystals after heterogeneously growing with ZnO nanoshell. *RSC Adv.* **2013**, *3*, 3309−3315.

(15) Yu, K.; Zeng, Y.; Wang, G.; Luo, X.; Li, T.; Zhao, J.; Qian, K.; Park, C. B. rGO/Fe3O4 hybrid induced ultra-efficient EMI shielding performance of phenolic-based carbon foam. *RSC Adv.* **2019**, *9*, 20643−20651.

(16) Liu, H.; Wu, J.; Zhuang, Q.; Dang, A.; Li, T.; Zhao, T. Preparation and the electromagnetic interference shielding in the X-band of carbon foams with Ni-Zn ferrite additive. *J. Eur. Ceram. Soc.* **2016**, *36*, 3939−3946.

(17) Yadav, R. S.; Kuřitka, I.; Vilcakova, J.; Machovsky, M.; Skoda, D.; Urbánek, P.; Masař, M.; Jurča, M.; Urbánek, M.; Kalina, L.; et al. NiFe2O4 Nanoparticles Synthesized by Dextrin from Corn-Mediated Sol-Gel Combustion Method and Its Polypropylene Nanocomposites Engineered with Reduced Graphene Oxide for the Reduction of Electromagnetic Pollution. *ACS Omega* **2019**, *4*, 22069−22081.

(18) Zachariah, S. M.; Grohens, Y.; Kalarikkal, N.; Thomas, S. Hybrid materials for electromagnetic shielding: A review. *Polym. Compos.* **2022**, *43*, 2507−2544.

(19) Chung, D. D. L. Materials for electromagnetic interference shielding. *Mater. Chem. Phys.* **2020**, *255*, 123587.

(20) Gupta, S.; Wei, C.-Y.; Tai, N.-H. Composition tunable manganese-doped magnetite microwave absorber composites for radio frequency identification communication. *Ceram. Int.* **2022**, *48*, 15105.

(21) Mohammed, J.; Trudel, T. T. C.; Hafeez, H.; Basandrai, D.; Bhadu, G. R.; Godara, S. K.; Narang, S.; Srivastava, A. Design of nano-sized Pr3+-Co2+-substituted M-type strontium hexaferrites for optical sensing and electromagnetic interference (EMI) shielding in Ku band. *Appl. Phys. A: Mater. Sci. Process.* **2019**, *125*, 1−12.

(22) Radoń, A.; Łukowiec, D.; Włodarczyk, P. Microwave absorption by dextrin-magnetite nanocomposite in frequencies below 2.5 GHz: Role of magnetite content, shape and temperature on magneto-dielectric properties. *Mater. Des.* **2020**, *193*, 108860.

(23) Singh, B.; Prasanta, V.; Choudhary, P.; Saini, S.; Pande, V.; Singh, R.; Mathur, R. B. Enhanced microwave shielding and mechanical properties of high loading MWCNT-epoxy composites. *J. Nanopart. Res.* **2013**, *15*, 1−12.

(24) Zhou, Y.; Deng, X.; Xing, H.; Zhao, H.; Liu, Y.; Guo, L.; Feng, J.; Feng, W.; Zong, Y.; Zhu, X.; et al. Dynamically observing the formation of MOFs-driven Co/N-doped carbon nanocomposites by in-situ transmission electron microscope and their application as high-efficient microwave absorbent. *Nano Res.* **2022**, *15*, 6819−6830.

(25) Sun, Y.; Zhang, J.; Zong, Y.; Deng, X.; Zhao, H.; Feng, J.; He, M.; Li, X.; Peng, Y.; Zheng, X. Crystalline-Amorphous Permalloy@ Iron Oxide Core-Shell Nanoparticles Decorated on Graphene as High-Efficiency, Lightweight, and Hydrophobic Microwave Absorbents. *ACS Appl. Mater. Interfaces* **2019**, *11*, 6374−6383.

(26) Sun, Y.; Wang, Y.; Ma, H.; Zhou, Y.; Xing, H.; Feng, W.; Feng, J.; Shi, Z.; Zong, Y.; Li, X.; et al. Fe3C nanocrystals encapsulated in N-doped carbon nanofibers as high-efficient microwave absorbers with superior oxidation/corrosion resistance. *Carbon* **2021**, *178*, 515−527.

(27) Qin, F.; Brosseau, C. A review and analysis of microwave absorption in polymer composites filled with carbonaceous particles. *J. Appl. Phys.* **2012**, *111*, 061301.

(28) Singh, K.; Ohlan, A.; Pham, V. H.; Varshney, S.; Jang, J.; Hur, S. H.; Choi, W. M.; Kumar, M.; Dhawan, S.; Kong, B.-S.; Chung, J. S. Nanostructured graphene/Fe3O4 incorporated polyaniline as a high performance shield against electromagnetic pollution. *Nanoscale* **2013**, *5*, 2411−2420.

(29) Dhawan, S. K.; Singh, K.; Bakhshi, A. K.; Ohlan, A. Conducting polymer embedded with nanoferrite and titanium dioxide nano-particles for microwave absorption. *Synth. Met.* **2009**, *159*, 2259−2262.

(30) Zahari, M. H.; Guan, B. H.; Cheng, E. M.; Che Mansor, M. F. C.; Lee, K. C. EMI shielding effectiveness of composites based on barium ferrite, PANI, and MWCNT. *Prog. Electromagn. Res. M* **2016**, *52*, 79−87.

(31) Cao, J.; He, P.; Mohammed, M. A.; Zhao, X.; Young, R. J.; Derby, B.; Kinloch, I. A.; Dryfe, R. A. Two-step electrochemical intercalation and oxidation of graphite for the mass production of graphene oxide. *J. Am. Chem. Soc.* **2017**, *139*, 17446−17456.

(32) Ojha, K.; Anjaneyulu, O.; Ganguli, A. K. Graphene-based hybrid materials: synthetic approaches and properties. *Curr. Sci.* **2014**, *107*, 397−418.

(33) Wang, B.; Wu, Q.; Fu, Y.; Liu, T. A review on carbon/magnetic metal composites for microwave absorption. *J. Mater. Sci. Technol.* **2021**, *86*, 91−109.

(34) Xiong, L.; Yu, M.; Liu, J.; Li, S.; Xue, B. Preparation and evaluation of the microwave absorption properties of template-free graphene foam-supported Ni nanoparticles. *RSC Adv.* **2017**, *7*, 14733−14741.

(35) Anand, S.; Pauline, S. Effective lightweight, flexible and ultrathin PVDF/rGO/Ba2Co2Fe12O22 composite films for electro-

magnetic interference shielding applications. *Nanotechnology* **2021**, *32*, 475707.

(36) Wang, X.; Yu, S.; Wu, Y.; Pang, H.; Yu, S.; Chen, Z.; Hou, J.; Alsaedi, A.; Hayat, T.; Wang, S. The synergistic elimination of uranium (VI) species from aqueous solution using bi-functional nanocomposite of carbon sphere and layered double hydroxide. *Chem. Eng. J.* **2018**, *342*, 321−330.

(37) Moslehi Niasar, M.; Molaei, M. J.; Aghaei, A. Electromagnetic Wave Absorption Properties of Barium Ferrite/Reduced Graphene Oxide Nanocomposites. *Int. J. Eng.* **2021**, *34*, 1503−1511.

(38) Qin, M.; Zhang, L.; Zhao, X.; Wu, H. Lightweight Ni Foam-Based Ultra-Broadband Electromagnetic Wave Absorber. *Adv. Funct. Mater.* **2021**, *31*, 2103436.

(39) Kukielski, M.; Bulejak, W.; Wiecinska, P.; Stobinski, L.; Slubowska, W.; Szafran, M. Graphene-reinforced ceramics obtained by slip casting and pressureless sintering: Interactions and stability of particles in aqueous environment. *Open Ceram.* **2022**, *9*, 100245.

(40) Liu, J.; Mckeon, L.; Garcia, J.; Pinilla, S.; Barwich, S.; Möbius, M.; Stamenov, P.; Coleman, J. N.; Nicolosi, V. Additive Manufacturing of Ti 3 C 2 -MXene-Functionalized Conductive Polymer Hydrogels for Electromagnetic-Interference Shielding. *Adv. Mater.* **2022**, *34*, 2106253.

(41) Wei, H.; Yu, Y.; Jiang, F.; Xue, J.; Zhao, F.; Wang, Q. Carbon@ SiC(SiCnws)-Sc2Si2O7 ceramics with multiple loss mediums for improving electromagnetic shielding performance. *J. Eur. Ceram. Soc.* **2022**, *42*, 2274−2281.

(42) Singh, J.; Bahel, S. Dielectric ceramics-based tunable and frequency-selective electromagnetic interference shields for next-generation applications. *J. Mater. Sci.: Mater. Electron.* **2021**, *32*, 16052−16068.

(43) Asthana, R.; Kumar, A.; Dahotre, N. B. Powder Metallurgy and Ceramic Forming. In *Materials Processing and Manufacturing Science*; Asthana, R., Kumar, A., Dahotre, N. B., Eds.; Academic Press: Burlington, 2006; pp 167−245.

(44) He, G.; Ding, J.; Zhang, J.; Hao, Q.; Chen, H. One-Step Ball-Milling Preparation of Highly Photocatalytic Active CoFe2O4-Reduced Graphene Oxide Heterojunctions For Organic Dye Removal. *Ind. Eng. Chem. Res.* **2015**, *54*, 2862−2867.

(45) Liu, S.; Dong, Y.; Zhao, C.; Zhao, Z.; Yu, C.; Wang, Z.; Qiu, J. Nitrogen-rich carbon coupled multifunctional metal oxide/graphene nanohybrids for long-life lithium storage and efficient oxygen reduction. *Nano Energy* **2015**, *12*, 578−587.

(46) Zhao, W.; Fang, M.; Wu, F.; Wu, H.; Wang, L.; Chen, G. Preparation of graphene by exfoliation of graphite using wet ball milling. *J. Mater. Chem.* **2010**, *20*, 5817−5819.

(47) Tan, H.; Navik, R.; Liu, Z.; Xiang, Q.; Zhao, Y. Scalable massive production of defect-free few-layer graphene by ball-milling in series with shearing exfoliation in supercritical CO2. *J. Supercrit. Fluids* **2022**, *181*, 105496.

(48) Keysight Instruments. *N1500A Materials Measurement Suite*; Keysight, 2020. Available at: https://www.keysight.com/ca/en/product/N1500A/materials-measurement-suite.html#Resources.

(49) Bartley, P. G.; Begley, S. B. A new technique for the determination of the complex permittivity and permeability of materials, *10th IEEE International Instrumentation and Measurement Technology Conference Proceedings*, 2010; pp 54−57.

(50) Sadek, R.; Sharawi, M. S.; Dubois, C.; Tantawy, H.; Chaouki, J. Superior quality chemically reduced graphene oxide for high performance EMI shielding materials. *RSC Adv.* **2022**, *12*, 22608−22622.

(51) Marcano, D. C.; Kosynkin, D. V.; Berlin, J. M.; Sinitskii, A.; Sun, Z.; Slesarev, A.; Alemany, L. B.; Lu, W.; Tour, J. M. Improved Synthesis of Graphene Oxide. *ACS Nano* **2010**, *4*, 4806−4814.

(52) Janasi, S.; Rodrigues, D.; Emura, M.; Landgraf, F. Barium Ferrite Powders Obtained by Co-Precipitation. *Phys. Status Solidi A* **2001**, *185*, 479−485.

(53) Jafari, A.; Farjami Shayesteh, S. F.; Salouti, M.; Boustani, K. Effect of annealing temperature on magnetic phase transition in Fe3O4 nanoparticles. *J. Magn. Magn. Mater.* **2015**, *379*, 305−312.

(54) Marinho, B.; Ghislandi, M.; Tkalya, E.; Koning, C. E.; de With, G. Electrical conductivity of compacts of graphene, multi-wall carbon nanotubes, carbon black, and graphite powder. *Powder Technol.* **2012**, *221*, 351−358.

(55) Ebara, H.; Inoue, T.; Hashimoto, O. Measurement method of complex permittivity and permeability for a powdered material using a waveguide in microwave band. *Sci. Technol. Adv. Mater.* **2006**, *7*, 77.

(56) Bai, Y.; Cai, H.; Qiu, X.; Fang, X.; Zheng, J. Effects of graphene reduction degree on thermal oxidative stability of reduced graphene oxide/silicone rubber nanocomposites. *High Perform. Polym.* **2015**, *27*, 997−1006.

(57) Manglam, M. K.; Kumari, S.; Mallick, J.; Kar, M. Crystal structure and magnetic properties study on barium hexaferrite of different average crystallite size. *Appl. Phys. A: Mater. Sci. Process.* **2021**, *127*, 1−12.

(58) Peternele, W. S.; Monge Fuentes, V.; Fascineli, M. L.; Rodrigues da Silva, J.; Silva, R. C.; Lucci, C. M.; Bentes de Azevedo, R. Experimental investigation of the coprecipitation method: An approach to obtain magnetite and maghemite nanoparticles with improved properties. *J. Nanomater.* **2014**, *2014*, 682985.

(59) Zhang, Y.; Yang, Z.; Pan, T.; Gao, H.; Guan, H.; Xu, J.; Zhang, Z. Construction of natural fiber/polyaniline core-shell heterostructures with tunable and excellent electromagnetic shielding capability via a facile secondary doping strategy. *Composites, Part A* **2020**, *137*, 105994.

(60) Koo, K. N.; Ismail, A. F.; Othman, M. H. D.; Bidin, N.; A Rahman, M. A. Preparation and characterization of superparamagnetic magnetite (Fe3O4) nanoparticles: A short review. *Malaysian J. Fundam. Appl. Sci.* **2019**, *15*, 23−31.

(61) Guimarães, A. P. Magnetism of Small Particles. In *Principles of Nanomagnetism*, 2nd ed.; Springer International Publishing: Cham, 2017; pp 71−124.

(62) Ling, J.; Zhai, W.; Feng, W.; Shen, B.; Zhang, J.; Zheng, W. G. Facile preparation of lightweight microcellular polyetherimide/graphene composite foams for electromagnetic interference shielding. *ACS Appl. Mater. Interfaces* **2013**, *5*, 2677−2684.

(63) Aliyev, E.; Filiz, V.; Khan, M.; Lee, Y.; Abetz, C.; Abetz, V. Structural characterization of graphene oxide: Surface functional groups and fractionated oxidative debris. *Nanomaterials* **2019**, *9*, 1180.

(64) Lim, Y.; Lai, C.; Hamid, S. B. A.; Julkapli, N. M.; Yehya, W.; Karim, M.; Tai, M.; Lau, K. A study on growth formation of nano-sized magnetite Fe3O4 via co-precipitation method. *Mater. Res. Innovations* **2014**, *18*, S6-457−S6-461.

(65) Ferrari, A. C.; Basko, D. M. Raman spectroscopy as a versatile tool for studying the properties of graphene. *Nat. Nanotechnol.* **2013**, *8*, 235−246.

(66) Thapliyal, V.; Alabdulkarim, M. E.; Whelan, D. R.; Mainali, B.; Maxwell, J. L. A concise review of the Raman spectra of carbon allotropes. *Diamond Relat. Mater.* **2022**, *127*, 109180.

(67) López-Díaz, D.; López Holgado, M.; García-Fierro, J. L.; Velázquez, M. M. Evolution of the Raman spectrum with the chemical composition of graphene oxide. *J. Phys. Chem. C* **2017**, *121*, 20489−20497.

(68) Dubey, V.; Kain, V. Synthesis of magnetite by coprecipitation and sintering and its characterization. *Mater. Manuf. Processes* **2018**, *33*, 835−839.

(69) Shebanova, O. N.; Lazor, P. Raman spectroscopic study of magnetite (FeFe2O4): a new assignment for the vibrational spectrum. *J. Solid State Chem.* **2003**, *174*, 424−430.

(70) Ohlan, A.; Singh, K.; Chandra, A.; Dhawan, S. Microwave absorption properties of conducting polymer composite with barium ferrite nanoparticles in 12.4-18GHz. *Appl. Phys. Lett.* **2008**, *93*, 053114.

(71) Yan, D.-X.; Ren, P.-G.; Pang, H.; Fu, Q.; Yang, M.-B.; Li, Z.-M. Efficient electromagnetic interference shielding of lightweight graphene/polystyrene composite. *J. Mater. Chem.* **2012**, *22*, 18772−18774.

(72) Yang, X.; Zhou, Y.; Xing, H.; Wang, H.; Feng, W.; Feng, J.; Zhu, X.; Shi, Z.; Zong, Y.; Li, X.; Zheng, X. MIL-88B (Fe) driven Fe/ Fe3C encapsulated in high-crystalline carbon for high-efficient microwave absorption and electromagnetic interference shielding. *J. Phys. D: Appl. Phys.* **2022**, *55*, 145003.

(73) Zhao, Z.; Lan, D.; Zhang, L.; Wu, H. A Flexible, Mechanically Strong, and Anti-Corrosion Electromagnetic Wave Absorption Composite Film with Periodic Electroconductive Patterns. *Adv. Funct. Mater.* **2022**, *32*, 2111045.

(74) Deng, W.; Li, T.; Li, H.; Liu, X.; Dang, A.; Liu, Y.; Wu, H. Controllable graphitization degree of carbon foam bulk toward electromagnetic wave attenuation loss behavior. *J. Colloid Interface Sci.* **2022**, *618*, 129−140.

(75) Hwang, U.; Kim, J.; Seol, M.; Lee, B.; Park, I.-K.; Suhr, J.; Nam, J.-D. Quantitative Interpretation of Electromagnetic Interference Shielding Efficiency: Is It Really a Wave Absorber or a Reflector? *ACS Omega* **2022**, *7*, 4135−4139.

(76) Wang, C.; Murugadoss, V.; Kong, J.; He, Z.; Mai, X.; Shao, Q.; Chen, Y.; Guo, L.; Liu, C.; Angaiah, S.; Guo, Z. Overview of carbon nanostructures and nanocomposites for electromagnetic wave shielding. *Carbon* **2018**, *140*, 696−733.

(77) Gill, N.; Sharma, A. L.; Gupta, V.; Tomar, M.; Pandey, O. P.; Singh, D. P. Enhanced microwave absorption and suppressed reflection of polypyrrole-cobalt ferrite-graphene nanocomposite in X-band. *J. Alloys Compd.* **2019**, *797*, 1190−1197.

(78) Gao, N.; Li, W.-P.; Wang, W.-S.; Liu, D.-P.; Cui, Y.-M.; Guo, L.; Wang, G.-S. Balancing Dielectric Loss and Magnetic Loss in Fe-NiS2/NiS/PVDF Composites toward Strong Microwave Reflection Loss. *ACS Appl. Mater. Interfaces* **2020**, *12*, 14416−14424.

(79) Zhao, Z.; Zhang, L.; Wu, H. Hydro/Organo/Ionogels: "Controllable" Electromagnetic Wave Absorbers. *Adv. Mater.* **2022**, *34*, 2205376.

(80) Liang, X.; Quan, B.; Chen, J.; Tang, D.; Zhang, B.; Ji, G. Strong electric wave response derived from the hybrid of lotus roots-like composites with tunable permittivity. *Sci. Rep.* **2017**, *7*, 9462.

(81) Xie, J.; Jiang, H.; Li, J.; Huang, F.; Zaman, A.; Chen, X.; Gao, D.; Guo, Y.; Hui, D.; Zhou, Z. Improved impedance matching by multi-componential metal-hybridized rGO toward high performance of microwave absorption. *Nanotechnol. Rev.* **2021**, *10*, 1−9.

(82) Afzali, S.-S.; Hekmatara, S. H.; Seyed-Yazdi, J.; Hosseini, S. M. B. M. Tuned MWCNT/CuO/Fe3O4/Polyaniline nanocomposites with exceptional microwave attenuation and a broad frequency band. *Sci. Rep.* **2022**, *12*, 9590.

(83) Jiang, D.; Murugadoss, V.; Wang, Y.; Lin, J.; Ding, T.; Wang, Z.; Shao, Q.; Wang, C.; Liu, H.; Lu, N.; et al. Electromagnetic Interference Shielding Polymers and Nanocomposites - A Review. *Polym. Rev.* **2019**, *59*, 280−337.

(84) Xie, P.; Li, H.; He, B.; Dang, F.; Lin, J.; Fan, R.; Hou, C.; Liu, H.; Zhang, J.; Ma, Y.; Guo, Z. Bio-gel derived nickel/carbon nanocomposites with enhanced microwave absorption. *J. Mater. Chem. C* **2018**, *6*, 8812−8822.

(85) Gairola, P.; Gairola, S. P.; Kumar, V.; Singh, K.; Dhawan, S. K. Barium ferrite and graphite integrated with polyaniline as effective shield against electromagnetic interference. *Synth. Met.* **2016**, *221*, 326−331.

(86) Ram, R.; Khastgir, D.; Rahaman, M. Physical properties of polyvinylidene fluoride/multi-walled carbon nanotube nanocomposites with special reference to electromagnetic interference shielding effectiveness. *Adv. Polym. Technol.* **2018**, *37*, 3287−3296.

(87) Mirkhani, S. A.; Arjmand, M.; Sadeghi, S.; Krause, B.; Pötschke, P.; Sundararaj, U. Impact of synthesis temperature on morphology, rheology and electromagnetic interference shielding of CVD-grown carbon nanotube/polyvinylidene fluoride nanocomposites. *Synth. Met.* **2017**, *230*, 39−50.

(88) Sambyal, P.; Dhawan, S. K.; Gairola, P.; Chauhan, S. S.; Gairola, S. P. Synergistic effect of polypyrrole/BST/RGO/Fe 3 O 4 composite for enhanced microwave absorption and EMI shielding in X-Band. *Curr. Appl. Phys.* **2018**, *18*, 611−618.

(89) Dalal, J.; Malik, S.; Dahiya, S.; Punia, R.; Singh, K.; Maan, A. S.; Dhawan, S. K.; Ohlan, A. One pot synthesis and electromagnetic interference shielding behavior of reduced graphene oxide nano-

composites decorated with Ni0.5Co0.5Fe2O4 nanoparticles. *J. Alloys Compd.* **2021**, *887*, 161472.

(90) Qiu, B.; Zhang, X.; Xia, S.; Sun, T.; Ling, Y.; Zhou, S.; Guang, H.; Chen, Y.; Xu, Z.; Liang, M.; et al. Magnetic graphene oxide/carbon fiber composites with improved interfacial properties and electromagnetic interference shielding performance. *Composites, Part A* **2022**, *155*, 106811.

(91) Zhao, B.; Zhao, C.; Li, R.; Hamidinejad, S. M.; Park, C. B. Flexible, Ultrathin, and High-Efficiency Electromagnetic Shielding Properties of Poly(Vinylidene Fluoride)/Carbon Composite Films. *ACS Appl. Mater. Interfaces* **2017**, *9*, 20873−20884.

(92) Al-Saleh, M. H.; Saadeh, W. H.; Sundararaj, U. EMI shielding effectiveness of carbon based nanostructured polymeric materials: a comparative study. *Carbon* **2013**, *60*, 146−156.

(93) Srivastava, R. K.; Xavier, P.; Gupta, S. N.; Kar, G. P.; Bose, S.; Sood, A. Excellent Electromagnetic Interference Shielding by Graphene- MnFe2O4-Multiwalled Carbon Nanotube Hybrids at Very Low Weight Percentage in Polymer Matrix. *ChemistrySelect* **2016**, *1*, 5995−6003.